RESEARCH ARTICLE | FEBRUARY 08 2024

Numerical study of Taylor bubble breakup in counter-current flow using large eddy simulation

Jan Kren ; E. M. A. Frederix ; Iztok Tiselj ; Blaž Mikuž

Physics of Fluids 36, 023311 (2024)
https://doi.org/10.1063/5.0186236

Numerical study of Taylor bubble breakup in counter-current flow using large eddy simulation

Cite as: Phys. Fluids **36**, 023311 (2024); doi: 10.1063/5.0186236
Submitted: 5 November 2023 · Accepted: 7 January 2024 ·
Published Online: 8 February 2024

Jan Kren,[1,2,a)] E. M. A. Frederix,[3] Iztok Tiselj,[1,2] and Blaž Mikuž[1]

AFFILIATIONS

[1]Reactor Engineering Division, Jožef Stefan Institute, Jamova cesta 39, Ljubljana 1000, Slovenia
[2]Faculty of Mathematics and Physics, University of Ljubljana, Jadranska ulica 19, Ljubljana 1000, Slovenia
[3]Nuclear Research and Consultancy Group (NRG), P.O. Box 25, Petten 1755 ZG, The Netherlands

[a)]Author to whom correspondence should be addressed: jan.kren@ijs.si

ABSTRACT

This paper investigates dynamics of Taylor bubble in counter-current flows, leveraging large eddy simulations combined with the volume of fluid method. Utilizing the OpenFOAM framework, we have implemented a high-order Runge–Kutta time-integration scheme, along with a piecewise linear interface calculation method for precise geometric reconstruction of the bubble interface. We examine the performance of algebraic vs geometric capturing techniques in the context of Taylor bubble breakup, focusing specifically on the transitional flow regime with a liquid Reynolds number of 1400. Our results reveal that the geometric capturing technique offers superior accuracy, improving our understanding of the breakup process and providing valuable insight for multiphase flow simulations in various engineering fields. Our study also reveals the emergence of a secondary vortex in the turbulent wake region behind the Taylor bubble, a phenomenon most prominent at finer mesh resolutions. This vortex represents a novel discovery in counter-current Taylor bubble flows.

I. INTRODUCTION

Understanding of phenomena in single-phase flows is in such a developed state that we can confidently construct new models that are sufficiently accurate for usage in complex flows.[1] However, in multiphase flows, this is not the case. There is still a significant lack of experimental data and theoretical knowledge to construct accurate tools for two-phase flows, especially for turbulent regime.[2,3] Two-phase slug flow is a prominent multiphase flow phenomenon with implications in a wide array of industrial and engineering applications, including oil and gas pipelines, chemical reactors, and nuclear reactors in normal operation and under accident management conditions. Characterized by the periodic formation of elongated gas bubbles or Taylor bubbles separated by liquid slugs, slug flow dynamics are influenced by numerous physical mechanisms, including interfacial surface tension, gravity, pressure gradients, and wall effects. Consequently, a comprehensive understanding of two-phase slug flow is not only fundamental to optimizing the design and operation of multiphase systems but also pivotal for accurate prediction of their performance under varying operating conditions. The importance of understanding and accurately predicting two-phase slug flows was underscored by the Deepwater Horizon explosion in 2010,[4] one of the most significant ecological disasters in recent history. An uncontrolled gas–liquid slug flow led to a catastrophic explosion, emphasizing the necessity for enhanced knowledge and predictive capabilities of such phenomena to prevent future disasters.

One of the central aspects of two-phase slug flow is bubble breakup, a phenomenon where a bubble fragments into smaller bubbles due to mechanisms such as turbulence, surface tension, and fluid viscosity.[5] Advancements in experimental and theoretical studies have illuminated the underlying physics of bubble breakup and spurred the development of sophisticated models. Yet, there remains a critical need for improved numerical methods capable of accurately simulating these intricate dynamics. Reliable experiments are crucial for development of the accurate databases, which can be used as a benchmark for numerical simulations. This is especially difficult for flows in the turbulent regime due to interactions between liquid and gas phases and the consequence of that—coalescence and breakup. Experimental studies of a Taylor bubble in turbulent flow are sparse, and most of them have been performed for co-current flow situations, where liquid flow and bubble buoyancy have the same direction.[6–10] The bubble's interface in turbulent flow exhibits unstable and chaotic flapping, which requires long time periods to obtain time-averaged picture.

As an alternative, a Taylor bubble in counter-current flow has been proposed, and it turned out that the bubble stays trapped in the equilibrium position for hours.[11,12] Experiments with the Taylor bubble in the counter-current regime were performed with a high-speed camera in visible light, and a disintegration rate of the bubble has been measured.[12] In a recent paper by Kren *et al.*,[13] the dynamics of the Taylor bubble interface were studied, which could also have implications on the bubble breakup and coalescence. The observed flow conditions are therefore suitable for studying the coalescence and breakup of gas bubbles.

Several other experiments of bubble breakup and coalescence have been made.[14] The measurements span from an investigation of the liquid film region during coalescence,[15,16] to the transition between flow patterns.[17] The recent development in the experimental methods using the multi-cameras approach enabled a better insight into the bubble breakup mechanisms and construction of new phenomenological models.[18] There are two review articles on bubble breakup models and mechanisms.[19,20] The first mechanism is breakup due to turbulent fluctuation and collision. In the turbulent case, the pressure fluctuations near the bubble–fluid interface and the collision between eddies and bubbles are the most common cause of breakup. The second mechanism is breakup due to viscous shear forces. These forces will induce a velocity gradient around the interface and deform the bubble, leading to breakup. As the bubble size increases, the leading cause of breakup is due to viscous shear. As the relative velocity between bubble and fluid increases, the skirt behind the bubble becomes unstable and starts breaking up. The last mechanism is breakup due to interfacial instability. This includes the Rayleigh–Taylor instability, which occurs when a lighter fluid is pushing the heavier one, and the Kelvin–Helmholtz instability, which occurs when there is a velocity shear in a single continuous liquid.

Numerical simulations of turbulent flows laden with droplets or bubbles can be carried out with different approaches. One possible option is Euler–Euler approach, where the Navier–Stokes equations are solved for each phase separately.[21] The other possible approach is one-fluid formulation, which consists of applying a single set of governing equations over the entire domain including the interface.[22] There are several methods for interface advection: the volume of fluid (VOF) method,[23,24] Front tracking method,[3] and level-set method[25] are among the most popular.

In this paper, we focus on the VOF method, which is implemented in the open-source OpenFOAM computer code.[26] An advantage of the VOF method over alternative methods is that it is already well established and conservation of volume is guaranteed. At the heart of the VOF method is the concept of a marker function that represents a volume fraction of one of the fluids in each computational cell of the domain. The basic problem with advecting a marker function is the numerical diffusion resulting from working with a cell-averaged marker function.[3] To prevent the marker function from further diffusion, the interface is reconstructed in the VOF method in such a way that the marker does not start to flow into a new cell until the current cell is full. The reconstruction methods are divided into algebraic and geometric reconstruction methods. Significant effort has been put into the application of the geometric methods as they show better results than the algebraic reconstruction methods.[27–29] One of such methods is Piecewise Linear Interface Calculation (PLIC) method, which has been investigated for large eddy simulations (LES) in the present study. LES offers a good compromise between precise and expensive DNS, and, cheap and less accurate RANS. The development of LES methods in multiphase flows is still in early stages, and one of the reasons for that is the lack of experimental and DNS benchmarks. The framework for the development of the LES in multiphase flows was proposed by Ketterl and Klein.[30,31] In single-phase flow, the modeling of small scales is needed only for the convective term, which is usually done by adding eddy viscosity to the equations. However, in multiphase flows, we need to model six terms, where at least two of them are significant. In general, the convective term can be modeled in the similar manner as in the single-phase flow,[32,33] but for other closures, new models need to be developed. The current status of development shows that the closure of the sub-grid term for surface tension is the most significant.[31,34–36]

Numerical simulations of a Taylor bubble were mainly studied in a stagnant or co-current background liquid flow in a variety of settings, from simple 2D and Euler–Euler simulations[37,38] to the full 3D simulations with interface tracking.[39,40] LES of the Taylor bubble in a co-current turbulent regime with no sub-grid scale models for bubble coalescence or breakup showed one to two orders of magnitude faster bubble disintegration than in the experiment of Taylor bubble in counter-current turbulent flow.[12,41] The phenomena that control the coalescence and breakup of bubbles are acting below the Kolmogorov scale and are therefore not directly incorporated in the formulation of the multiphase flow equations.[3] However, performing DNS or LES with interface tracking allows for coalescence and breakup by design, but it is usually not physically accurate due to various reasons. The VOF method, for example, has issues with calculating the curvature from the front using volume fractions. For coalescence cases, the problem with the VOF method is that it cannot distinguish between two interfaces in the same cell so a multi-marker method is needed. Additional models therefore need to be applied. For the level-set method, a model that prevents or delays bubble coalescence has been constructed and applied successfully to the numerical simulations.[42] Other models have been proposed for the coalescence and breakup using combined level-set and VOF method[43] and the immersed boundary method[44] with limited success. To sum up, the work on experimental and numerical gas–liquid turbulent flows has been extensive, but it is still lacking on several aspects of understanding the phenomena.

Despite the extensive body of literature on Taylor bubble flows and breakup dynamics, there remains a notable gap in high-fidelity numerical studies that focus on the breakup of Taylor bubbles in counter-current flow regimes. Previous research has often employed simplified models or lower-fidelity simulations, which may not fully capture the complex interplay of fluid dynamics phenomena such as coalescence and breakup. Our study aims to bridge this gap by employing large eddy simulation (LES) techniques with algebraic and geometric VOF to provide a more accurate and comprehensive understanding of Taylor bubble dynamics in counter-current flows.

The paper is structured as follows: following this introduction, we present the theoretical background and the numerical methodology employed (Sec. II), including the implementation and coupling of the Runge–Kutta (RK) and PLIC methods. In Sec. III, we compare the performance of algebraic vs geometric capturing techniques for the Taylor bubble scenario, especially for transitional flow with a Reynolds number of 1400 (see Sec. III). We also present detailed results for the

geometric VOF simulations. In Sec. IV, we show the implications of currently developed techniques for Taylor bubble flow at higher Reynolds number 5600 (Sec. IV). We specifically highlight and critically examine some limitations of our model. While the model demonstrated efficacy for simulations of transitional flow, it shows inadequacies when applied to turbulent conditions where bubble breakup is more pronounced. Notably, in the context of Taylor bubbles in counter-current turbulent flow, two key physical phenomena become increasingly significant: the enhanced breakup of the bubble and the asymmetry in the bubble's shape and behavior, which the model fails to correctly predict. We conclude the paper by discussing the implications of our findings and suggesting future research directions. In the Appendix, complete validation of the numerical framework with the Hysing rising bubble case and Zalesak slotted disk case is presented.

II. METHODOLOGY

A two-phase gas–liquid system has been modeled using the one-fluid formulation of the Navier–Stokes equations and the VOF approach for interface capturing. Within this framework, a void fraction, denoted as α, is defined. Its advection equation is given as

$$\partial_t \alpha + \mathbf{u} \cdot \nabla \alpha = 0, \tag{1}$$

where ∂_t is the time derivative, $\mathbf{u}$ is the velocity vector, and ∇ is the gradient operator. The fluid mixture's behavior is governed by the incompressible Navier–Stokes equations, represented as

$$\nabla \cdot \mathbf{u} = 0 \tag{2}$$

and

$$\partial_t(\rho \mathbf{u}) + \nabla \cdot (\rho \mathbf{u}\mathbf{u}) = -\nabla p + \rho \mathbf{g} + \nabla \cdot (2\mu_{eff}\mathbf{D}) + \sigma \boldsymbol{\kappa}\boldsymbol{\delta}(\mathbf{n})\mathbf{n}, \tag{3}$$

where $\rho = \alpha\rho_1 + (1-\alpha)\rho_2$ is the mass density, p is the pressure, $\mathbf{g}$ is the gravitational acceleration, $\mathbf{D}$ is the deformation tensor, $\mu_{eff} = \alpha\mu_1 + (1-\alpha)\mu_2$ is the effective mixture viscosity, $\boldsymbol{\kappa}$ is the interface curvature, $\mathbf{n}$ is the interface normal unit vector, and $\boldsymbol{\delta}(\mathbf{n})$ represents the interface Dirac delta function. These equations are solved in the open-source computational fluid dynamics (CFD) software OpenFOAM v10, with the aid of a modified interFoam solver. The solver enables the usage of Diagonally Implicit Runge–Kutta (DIRK) time integration schemes integrated with PLIC geometric reconstruction. It is an extension of a solver developed previously in OpenFOAM v4 by Frederix *et al.*[45] The subgrid-scale model used in the present work is eddy viscosity model WALE (Wall-Adapting Local Eddy-viscosity).[1] The Pressure-Implicit with Splitting of Operators (PISO) algorithm is employed to find the solution to the system of governing equations. Unlike coupled methods, the PISO technique decouples the equations for pressure and velocity, solving them in a segregated manner. Within this framework, two inner corrector loops are utilized. This implies that the equation for pressure is formulated and solved on two separate occasions within each Runge–Kutta (RK) stage of the time-stepping scheme. Surface tension term is being solved in the OpenFOAM using continuum surface tension model (CSF) as described by Brackbill *et al.*,[46] which smears the surface tension force over multiple cells, using a Dirac delta function, where $\delta(x) = \nabla\alpha$. The Dirac-delta function in the surface tension term is being smoothened with the help of the α function. Goal is to achieve exact balance between the pressure gradient and the surface tension forces.

The key component of this study is the comparison between the algebraic and geometric VOF method. Until OpenFOAM v8, only an algebraic VOF method was implemented. In our current study, we have implemented the Runge–Kutta time-integration scheme in the interFoam solver of OpenFOAM v10, which has implemented the PLIC method, i.e., a geometric VOF method.

A critical component of the algebraic VOF method is the accurate computation of the numerical fluxes to update the void fraction function.[3] Originally, a donor–acceptor formulation, along with flux limiters, was employed to ensure the boundedness of the α function. In OpenFOAM v10, algebraic capturing is performed through the Multidimensional Universal Limiter for Explicit Solution (MULES) framework.[26] It uses Flux Corrected Transport (FCT) with an interface compression scheme.

The geometric VOF method, on the other hand, involves a two-step process for interface reconstruction and advection, following Dai and Tong.[28] The interface approximation is first geometrically built from volume fraction information. This is typically accomplished using methods like the PLIC interface reconstruction. The reconstructed interface is then advected using the given velocity field. For the PLIC methods, the reconstruction process involves determining the normal from the known α function within the cell and its neighbors using a gradient of the α field. Geometrically, the line is then moved in the normal direction so that the interface position in each cell aligns with the local void fraction value. In OpenFOAM, the PLIC method is employed to compute the fluxes, after which the α equation is algebraically solved. This approach sets OpenFOAM apart from the typical methods adopted by other CFD codes. MULES framework is also used with the PLIC method to ensure local volume enforcement.

For the spatial discretization of the divergence terms, we rely on Gauss' theorem, which, in the finite volume framework, reduces to a simple summation of all the face-normal fluxes across all the faces enclosing each control volume. Similarly to Frederix *et al.*,[45] we have used blended scheme for momentum convection term that stabilizes the artificial breakup and does not have a detrimental effect on the single-phase turbulence far away from the bubble. All other interpolations and gradients are discretized using linear schemes, which are second-order accurate. The modified solver is able to use any Runge–Kutta scheme, but we have mainly used the Diagonally Implicit Runge–Kutta scheme of second order (DIRK2). Butcher tableau, which is Runge–Kutta matrix for coefficients for each Runge–Kutta stage and term, for this scheme is the following:[47]

$$\begin{array}{c|cc} \gamma & \gamma & 0 \\ 1 & 1-\gamma & \gamma \\ \hline & 1-\gamma & \gamma \end{array} \tag{4}$$

where $\gamma = 1 - \frac{\sqrt{2}}{2}$. Time-step was used in such a manner that the CFL number was below 0.4. Additionally, given the Weber number for this scenario, the constraint on the time step imposed by the surface tension term is less stringent. The complete verification of our solver can be found in the Appendix.

We have chosen fluid properties that resemble a water–air mixture and simulated Taylor bubble motion under two conditions—a pipe with a diameter of 12.4 mm (transitional flow) and another with a diameter of 26 mm (turbulent flow). These two cases were chosen as

TABLE I. Dimensionless numbers for the transitional and turbulent case.

Case	Morton	Froude	Eötvos	Weber	Reynolds
Transitional	2.60×10^{-11}	0.069	19.34	1.33	1400
Turbulent	2.60×10^{-11}	0.113	90.90	10.4	5600

the same setup is being used in experimental measurements in the THELMA laboratory of Reactor Engineering Division, Jožef Stefan Institute. It should be noted that forces acting on the Taylor bubble in counter-current flow are buoyancy, liquid velocity, surface tension, and liquid inertia. The bubble in that conditions is in inertial regime, which means that viscosity and surface tension effects can be neglected and the bubble rising velocity in stagnant liquid can be approximated with $U = k\sqrt{(gD)}$, where k is experimentally deduced constant and D is pipe diameter.

Our analysis focuses on a water–air mixture at 20 °C, the behavior of which can be better understood through several dimensionless numbers, as presented in Table I. We calculated the Weber, Eötvös, Froude, and Morton numbers for two cases characterized by terminal velocities of 0.09 and 0.17 m/s and characteristic lengths (pipe diameter) of 0.0124 and 0.026 m, respectively. The Weber number, which provides a ratio of inertial forces to surface tension forces, is crucial in predicting the formation and breakup of bubbles in a fluid. The Eötvös number, comparing buoyancy to surface tension forces, is instrumental in understanding the rise or fall of bubbles in a fluid. The Froude number, which compares the flow inertia to the external field (typically gravity), is key in predicting the formation of waves and overall fluid flow patterns. Finally, the Morton number, which characterizes the motion of bubbles or drops in a surrounding fluid, is essential in predicting the shape and behavior of bubbles, taking into account the properties of both fluids, including their viscosity, density, and surface tension. These dimensionless numbers again prove that we are in the inertial bubble regime as the inertial forces dominate over surface tension and liquid viscosity.

$$\text{Weber number (We)} \qquad \text{Eötvö snumber(Eo)}$$

$$We = \frac{\rho D U^2}{\sigma} \qquad Eo = \frac{(\rho_L - \rho_G) g D^2}{\sigma}$$

$$\text{Froude number (Fr)} \qquad \text{Morton number (Mo)}$$

$$Fr = \frac{U}{\sqrt{gD(\rho_L - \rho_G)/\rho_L}} \qquad Mo = \frac{g\mu^4(\rho_L - \rho_G)}{\rho_L^2 \sigma^3}$$

Pertinent issue in the numerical simulations of two-phase flows is spurious currents, which are also observable in the OpenFOAM computer code. The surface tension term is in OpenFOAM calculated as continuum surface tension force. According to Abadie *et al.*[48] and Popinet,[49] this method has a large span of sensitivity to spurious currents, which are important, particularly when the capillary forces are dominant, i.e., usually for Capillary number $Ca \ll 1$ and Weber number $We \ll 1$. However, in the current regime, where We number is 1.33 (Transitional case) and 10.4 (Turbulent case) and the flow is inertia dominant, the spurious currents are negligible. Spurious currents would be more prominent in the case of Taylor bubbles in microchannels and/or at smaller streamwise velocities.

In order to simulate the Taylor bubble in counter-current flow situation and under fully developed turbulent conditions, we applied a recycling boundary condition at the inlet, positioned upstream of the Taylor bubble. The recycling is done five hydraulic diameters D_h after the inlet. This way we ensure that the velocity field has enough space to fully develop.[50] After the recycling, there is another 2–3D_h to the Taylor bubble nose to ensure that the nose does not influence the recycling boundary condition. We adjusted the flow rate at every time step to balance the bubble's buoyancy with hydrodynamic drag, ensuring the bubble's position remains relatively constant throughout the simulation. This procedure is illustrated in Fig. 1. Small changes were adjusted with a gentle relaxation factor of 0.01 to keep the bubble from being pushed one way or another due to minor fluctuations. Velocity at the inlet at each time step was prescribed as

$$U_{inlet}^{k+1} = U_{inlet}^{k} - 0.01 U_{TB}, \tag{5}$$

where U_{TB} is the velocity of the Taylor bubble and we aim for it to be 0.

We conducted the study of $Re = 1400$ cases on three different mesh resolutions, as shown in Fig. 2. The geometry of all the meshes was identical: a cylinder with a length of 0.248 m and a diameter of 12.4 mm. The G20 mesh has around 700 000 hexahedral cells, the G15 mesh around 2×10^6 cells, and the G10 mesh 4.1×10^6 cells. The numerical designation in each mesh name corresponds to the dimensionless spanwise bulk cell size. In the near-wall region, the dimensionless spanwise cell size reduces to below 1 wall unit. Wall unit spacing is defined as $\delta x^+ = \delta x U^*/\nu$, where δx is the width of the cell in dimension units, U^* is the friction velocity, and ν is the kinematic viscosity. The friction velocity was determined in the wake region behind the Taylor bubble, where it attains its maximum value. Meanwhile, in the streamwise direction, the cell size is roughly equivalent to that in the bulk spanwise direction, albeit with minor refinement in the near-bubble region. More information about the meshes can be found in Table II.

III. RESULTS: TAYLOR BUBBLE IN TRANSITIONAL COUNTER-CURRENT FLOW

In this section, we present LES results of a Taylor bubble in the counter-current flow regime. We focus on a pipe with a 12.4 mm

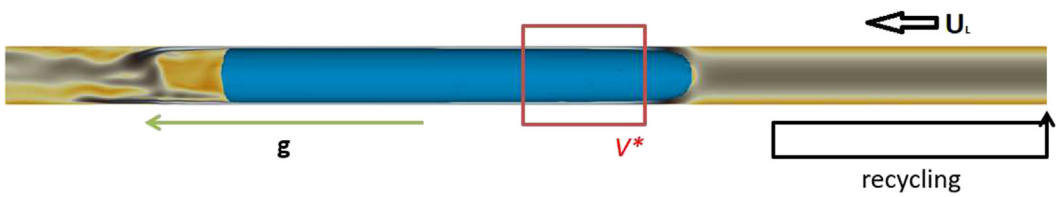

FIG. 1. Visualization of the recycling procedure. The bubble motion was calculated for every time step in the volume V^* and the flow rate has been adjusted accordingly.

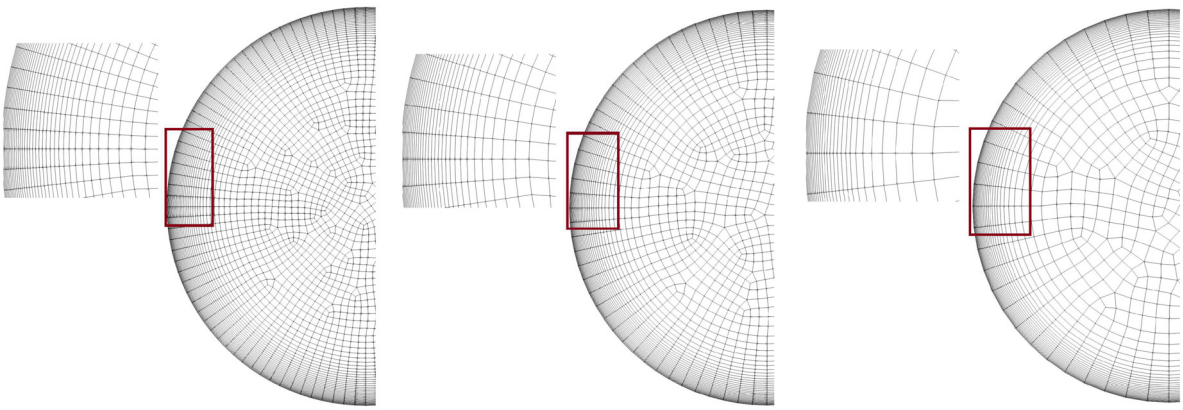

FIG. 2. Three different mesh resolutions: G10 (left), G15 (middle), and G20 (right).

diameter, where the liquid Reynolds number upstream of the Taylor bubble is approximately 1400, corresponding to laminar flow conditions. However, as the liquid water accelerates around the Taylor bubble and detaches at the trailing edge of the Taylor bubble, turbulence is generated. Consequently, we refer to this case as a Taylor bubble in a transitional flow regime. Our study primarily examines the shape, velocity, and breakup dynamics of the Taylor bubble, shedding light on the impact of the liquid flow regime on the bubble breakup process. In addition, the comparison of two different interface capturing schemes is shown, i.e., the algebraic and geometric (PLIC) reconstruction.

Importantly, our simulations are validated against experimental results from our laboratory that investigate Taylor bubbles in countercurrent flows at varying lengths.[12] It is worth noting that while bubble void shedding is a key characteristic in such flow conditions, its occurrence is proportional to the bubble length. It should be stressed that in the cases considered in the present study, there was practically no void shedding observed in experiments.

A. Validation with experiment

Liquid film thickness measurements were performed using the method presented in Kren *et al.*[13] This section provides a brief quantitative comparison with the experiment, thereby validating our numerical methods. The simulated bubbles are compared with the most relevant experimental bubble. In Fig. 3, the bubble shape and liquid film thickness are observed. This comparison presents a significant challenge for the VOF method as the interface shape is more distorted compared to the level-set or, notably, the front-tracking method. However, as shown in Fig. 3, there is excellent agreement in shape between the experimental and simulation results, for both algebraic and geometric VOF methods. The experimental results are displayed with a 5% error margin, indicated by the shaded region around the data points. The bubble shape is a critical characteristic as it affects the pressure drop induced by the bubble as well as the flow properties in the wake. The first and second profile denoted in Fig. 3 correspond to the left and right profile of the Taylor bubble based on the Taylor bubble nose, which is on the centerline due to bubble symmetry.

TABLE II. Properties of the meshes. Cell sizes are in wall units.

	Mesh G20	Mesh G15	Mesh G10
Wall-normal wall cell size	0.6	0.6	0.6
Spanwise bulk cell size	20	15	10
Inlet/outlet streamwise cell size	35	24	18
Bubble region streamwise cell size	17	11	8
Domain length	20D	20D	20D
Domain diameter (mm)	12.4	12.4	12.4
Number of cells	0.75×10^6	2.05×10^6	4.2×10^6
Number of cells inside Taylor bubble	0.25×10^6	0.8×10^6	2×10^6

B. Instantaneous fields

Figure 4 illustrates the isosurfaces of instantaneous gas void fraction at $\alpha = 0.5$ for the two distinct interface capturing methods, captured at three different time instances: $t = 5$ s, $t = 10$ s, and $t = 15$ s. On the right side, a photo from experimental observations shows a Taylor bubble of comparable length. There is a noticeable void

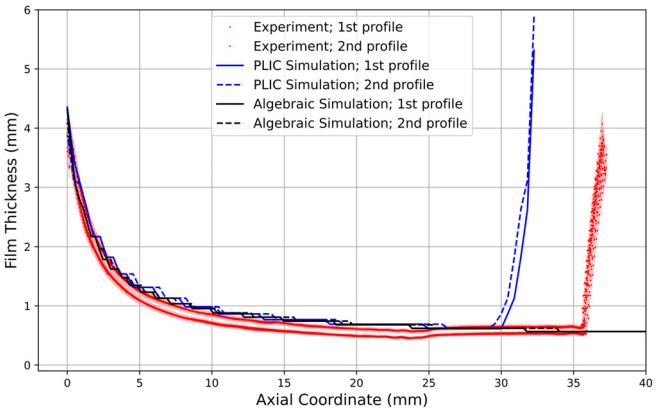

FIG. 3. Comparison of the experimental and numerical bubble shape.

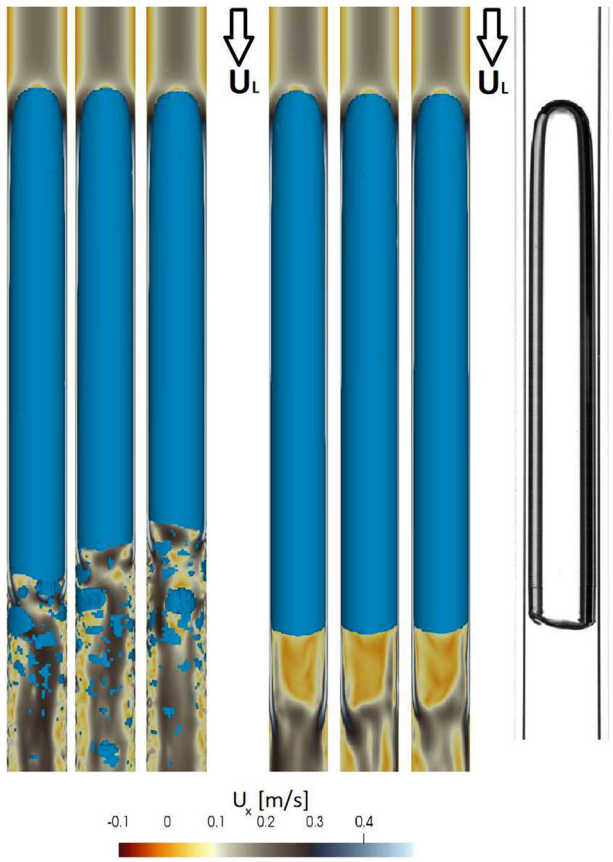

FIG. 4. Isosurfaces of the instantaneous gas void fraction (blue color) at three different timesteps ($t = 5$, $t = 10$, and $t = 15$ s) obtained with standard algebraic interface capturing (left) and PLIC reconstruction (middle) for transitional case ($Re = 1400$). The color scheme in the liquid phase represents the velocity magnitude. On the right side is the experimental measurement of Taylor bubble in counter-current flow.

shedding exhibited in the case of the algebraic VOF method. In contrast, the geometric VOF method does not display this behavior. This is first evidence that the geometric VOF method shows better agreement with the experimental observations.[12] Furthermore, a stark difference between the algebraic and geometric VOF methods is identified in the velocity fields within the bubble's wake region, as illustrated in Fig. 4. In the case of the geometric VOF method, the wake region presents an organized pattern, characterized by recirculating flow patterns that trail the bubble. On the other hand, the algebraic VOF method produces a starkly contrasting scenario. The wake region in this instance is punctuated by a higher degree of disorder. Numerous smaller bubbles emerge and proliferate, causing significant perturbations to the velocity field. These multiple smaller bubbles contribute to a more random and turbulent flow pattern, making the velocity field more chaotic.

In Table III, the average loss of void fraction (gas) is compared across different mesh sizes and interface capturing methods. For the algebraic method, the loss of void fraction decreases as the mesh becomes finer. As mentioned in the beginning, the void shedding has

TABLE III. Average loss of void fraction (gas) for different meshes and interface capturing methods.

	Algebraic	PLIC
G20	0.112 cm^3/s	0
G15	0.0659 cm^3/s	0
G10	0.0615 cm^3/s	0

not been experimentally observed for this particular case;[12] thus, we believe the observed loss void fraction in the algebraic exhibit artificial numerical breakup. In contrast, the PLIC method shows no loss of void fraction across all mesh sizes. This is desirable as we have been able to stop the artificial numerical breakup.

These results demonstrate the importance of the choice of interface capturing method in simulations of multiphase flow, particularly for cases where the bubble void shedding is of interest. The algebraic VOF method, while simpler and less computationally intensive, may lead to artificial bubble fragmentation due to its less accurate representation of the interface. On the other hand, the PLIC method provides a more accurate prediction of the bubble void shedding, but at a higher computational cost. Therefore, the choice between these two methods will depend on the specific requirements of the simulation. Enhanced bubble fragmentation also affects other hydrodynamic properties, such as velocity fields, velocity fluctuations, and turbulent kinetic energy (TKE). For these reasons, we have demonstrated that the PLIC method is superior for this case. Therefore, in Secs. III C and III C 1, we focus solely on simulations conducted using the PLIC method.

C. Time-averaged fields

At the bubble wake region, the flow is actually not laminar, but chaotic. Thus, time-averaging is needed to obtain comparable data that we provide in this section. By presenting the time-averaged fields, we aim to give a comprehensive overview of the differences in the flow characteristics predicted by the PLIC method on different meshes. The length of the time-averaging for different cases can be seen in Table IV. It turned out that sufficient statistical accumulation is about 50 s; however, we afforded longer time-averaging especially for the PLIC method due to no loss of void fraction. All simulations were conducted on in-house computer cluster, utilizing 100–300 CPUs depending on the mesh size. One single simulation on our finest mesh reproduced 50 s of statistical accumulation in about one month.

Figure 5 represents the 2D contour plots of mean streamwise, radial, and tangential velocities, respectively. The streamwise velocity contour illustrates the flow along the direction of the main flow.

TABLE IV. Time-averaging of different simulations.

Mesh \ Model	PLIC
G20	380 s
G15	150 s
G10	70 s

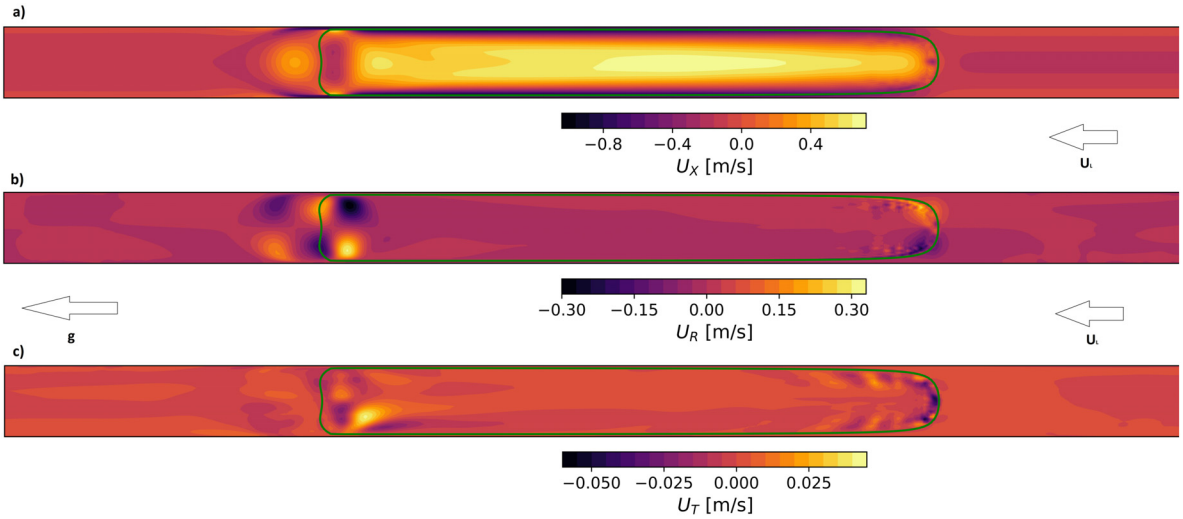

FIG. 5. 2D velocity fields of streamwise (a), radial, (b) and tangential velocity (c) at the middle plane of the pipe along with the mean position of the bubble denoted with green line. The results are from coarse G20 mesh with the PLIC method.

Notice the larger velocities in the annular region surrounding the bubble and slower streamwise velocities in the wake region, a typical characteristic of the Taylor bubble flow regime. The radial velocity contour provides insight into the flow direction concerning the bubble's center. The most flapping of the velocity is observed in the bubble wake region, where there is a pronounced recirculation zone. In the radial velocity field, there is a visible "checkerboard" pattern that shows coupling between the velocity inside the Taylor bubble and in the bubble wake region. The bottom contour in Fig. 5 presents the tangential velocity component, which is the smallest in magnitude. Here, the near-zero tangential velocity along the interface signifies that there is a minimal rotational or swirl motion about the bubble axis which could be also due to computational instabilities. However, as the magnitude is very small, this is still indicative of the axisymmetric nature of the flow around the Taylor bubble in the transitional regime.

Figure 6 presents time-averaged one-dimensional plots providing more detailed information on the streamwise velocity at five different cross sections. Five distinct graphs are shown with three different meshes on each graph. Clearly, there is no significant difference between the meshes for single-phase laminar flow upfront the bubble (cyan profile). However, the discrepancies are observed between all three simulations at the tip of the nose profile (red profile). It should be noted that these differences stem from the fact that the Taylor bubble is slightly moving during time-averaging and our reference point at the tip of the bubble is at different location for each simulation. Thus, there is a small uncertainty of the reference point location which is associated with its detection criteria, time-averaging, and spatial discretization. In the film region (green profile), we observe very good agreement and the highest velocities correspond to the location of gas–liquid interface (dotted-dashed line). However, there are some discrepancies inside the bubble (shaded red area) in the core region of the pipe, which can be attributed to insufficient spatial resolution of the coarsest mesh. In the bubble wake region (indicated by the yellow line), significant differences are observed with varying meshes. This variation can be attributed to the critical influence of the bubble's position on this velocity profile as seen in Fig. 5. Further downstream the turbulent flow slowly laminarizes; however, the velocity profile at the blue profile is still chaotic. The simulations at this location predict consistent velocity profiles with minor asymmetries.

The velocity fluctuation contours can be found in Fig. 7. As the velocity fluctuations span over a large range in magnitude, we have plotted it with log scale colorbar. Due to the interaction between the bubble and the incoming fluid, the flow generates turbulence, and in the bubble wake region, the fluctuations are significantly larger. These fluctuations are orders of magnitude larger than in other regions. The largest fluctuations are in the streamwise direction; however, the peak is in the small region near the flow separation region. More spatially pronounced are the radial velocity fluctuations, but they are an order of magnitude smaller than the maximum value in the streamwise direction. Here, we also observe the coupling between the velocity field in the wake and the velocity field inside the tail of the bubble, where the fluctuations are the largest in magnitude. The tangential fluctuations are the smallest in magnitude, which again shows the axisymmetric nature of the Taylor bubble in transitional regime. The last graph in Fig. 7 shows the turbulent kinetic energy (TKE), which combines the strongest structures of each of the velocity fluctuations field. Turbulent kinetic energy is calculated as $TKE = \frac{1}{2}(U'^2_{XX} + U'^2_{RR} + U'^2_{TT})$. We observe a noticeable increase in TKE at the interface between the bubble and the surrounding liquid, especially toward the rear of the bubble. This could be indicative of high turbulence production at the interface due to the shear between the bubble and the downward flow.

These findings are significant as they enhance our understanding of the local flow characteristics around Taylor bubbles and the role of turbulence as a precondition for bubble breakup and coalescence. The observed distribution of TKE also aligns with previous experimental and computational studies in co-current regime,[51] which have reported heightened turbulence activity near the bubble–liquid interface.

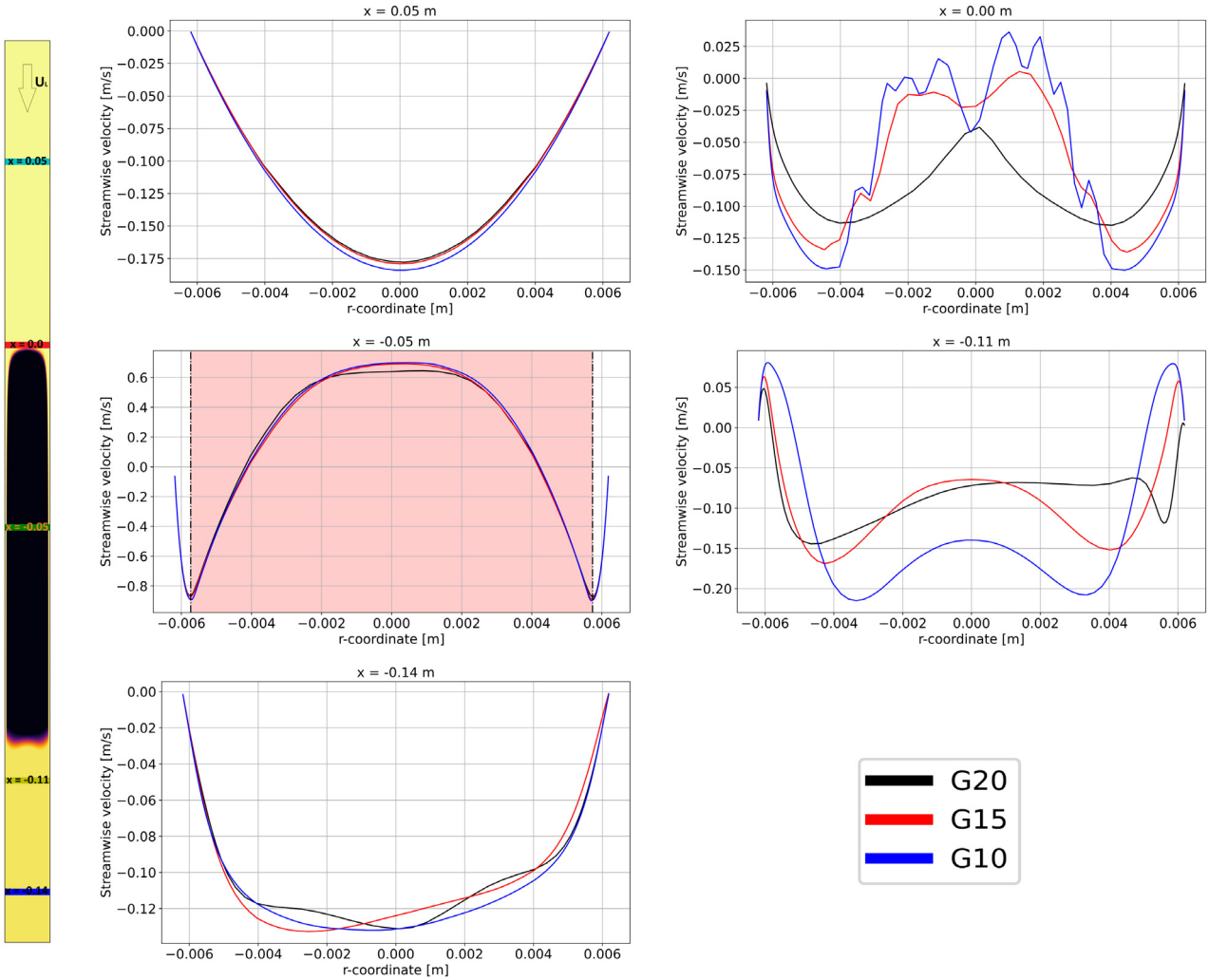

FIG. 6. Streamwise velocity profile of a Taylor bubble in counter-current flow. The left side of the figure presents a 2D schematic of a Taylor bubble with denoted different cross sections. The right side displays five one-dimensional plots of streamwise velocity, arranged in two rows, corresponding to the cross sections around the Taylor bubble.

Figure 8 presents one-dimensional profiles of streamwise velocity fluctuations. Upstream the Taylor bubble the flow is laminar; hence, very low fluctuations are observed. The velocity fluctuations develop in the vicinity of the Taylor bubble nose, in particular inside the bubble, and increase downstream the flow. The largest values occur inside the bubble and inside its wake region. Minor differences exist between the different used meshes. The coarsest G20 mesh consistently displays reduced fluctuations in all profiles, underscoring the importance of utilizing fine mesh discretization.

Similar trends can also be observed for the radial velocity fluctuations in Fig. 9. Following the film region, we detect a liquid jet, also visible in Fig. 5. In this area, we accordingly note the most substantial velocity fluctuations within the liquid region. Again, we observe minor differences between meshes. Nevertheless, the discrepancies between results are small and could be attributed to the uncertainty of the reference coordinate point at the tip of the bubble, similarly as in velocity profiles.

Turbulent kinetic energy is calculated as the sum of each component of velocity fluctuations. Consequently, the patterns observed in Figs. 8 and 9 are similar to the TKE calculations in Fig. 10. While disparities among the meshes are noticeable, they can again be attributed to the error of bubble nose position. Interestingly, we observe large sharp peaks of TKE in the gas–liquid interface region, in particular in the gas phase side. TKE slowly decreases in the bubble wake region, where TKE has lower values and dissipates faster downstream the bubble. Again, the coarsest G20 mesh shows the lowest values of TKE.

1. Turbulent wake region

The turbulent wake region behind a Taylor bubble in a counter-current flow exhibits characteristics, which are to some extent similar to the flow behind a backward-facing step.[52] Namely, in both cases, there is a flow separation region, which shares a common trait: the

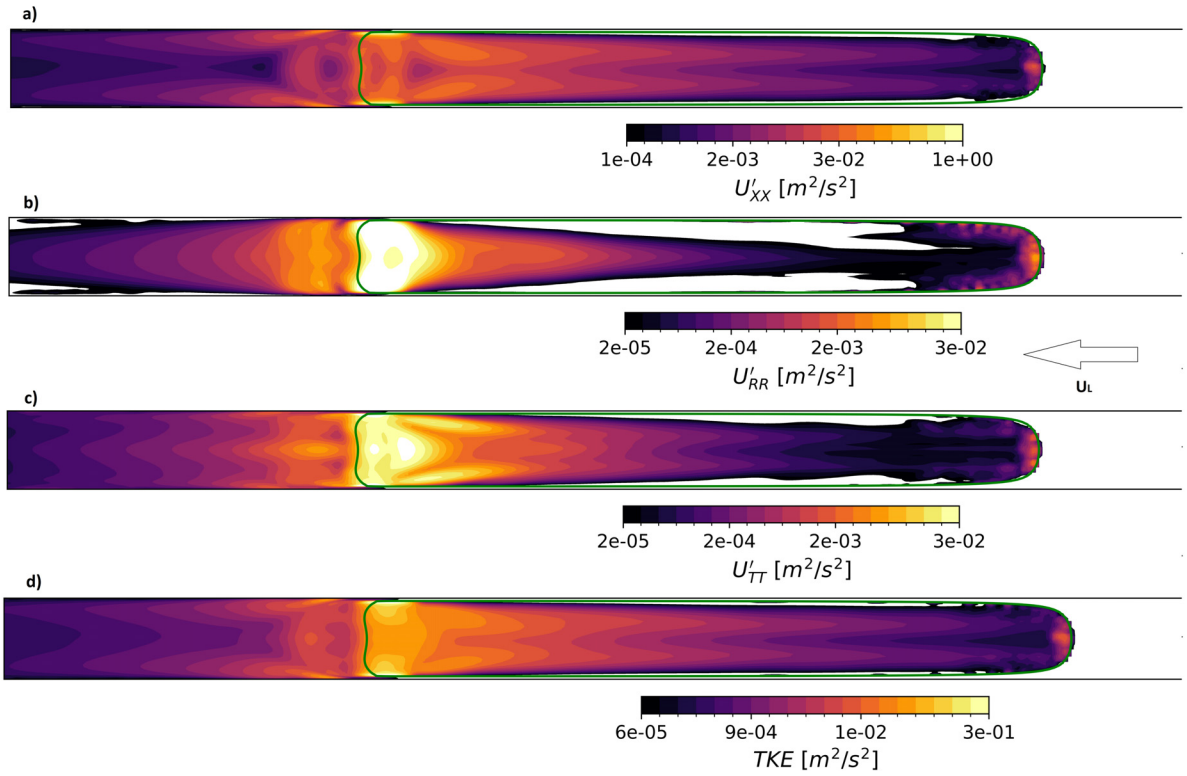

FIG. 7. 2D velocity fluctuations fields of streamwise (a), radial (b), tangential velocity fluctuations, (c) and turbulent kinetic energy (d) along with the mean position of the bubble denoted with green. The results are from coarse G20 mesh with PLIC method.

abrupt change in the flow direction, which leads to a strong deceleration of the fluid and eventually to the formation of a recirculation zone behind the bubble as shown in Fig. 11. However, there is also a distinct difference between both cases. First, the recirculation zone downstream the Taylor bubble has a toroidal shape due to the axial symmetry and, second, there is a secondary toroidal vortex observed besides the primary toroidal vortex as shown in Fig. 11. The secondary vortex has been successfully reproduced on the G15 and G10 meshes, while the reproduction on the coarsest G20 mesh is only partial. Thus, the prediction of the secondary toroidal vortex is quite sensitive to the spatial resolution of the mesh despite the fact that the magnitude of that vortex is not weak. This phenomenon is novel in the Taylor bubble in counter-current flow regime and, as far as we are aware, has not been highlighted in prior studies. The primary vortex, labeled in Fig. 11, aligns with what has been traditionally observed in both stagnant and co-current flow regimes of Taylor bubble flow. Quantitatively, the magnitude of this secondary vortex is about four times smaller than its primary counterpart.

Figure 12 presents three distinct fields. The top graph displays the streamwise velocity along the pipe's axis, while the middle graph illustrates the fluctuations of the streamwise velocity at the same location, and the bottom graph depicts radial velocity fluctuations. These graphs provide a clear understanding of how the velocity fields are affected by the presence of the bubble. A consistent pattern emerges throughout the graphs. Namely, upstream the Taylor bubble, the flow is laminar, and the fluctuations steeply intensify as the bubble's interface is approached. Then, inside the bubble, the fluctuations are rather low, but they again increase in the vicinity of the trailing edge interface of the bubble. Here, the distinct peaks of velocity fluctuations with the largest magnitudes are observed. Following the bubble's passage, the fluctuations slowly laminarize downstream the Taylor bubble. Clearly, this transition process exhibits some dependence on mesh resolution, particularly in terms of turbulence amplitude at different sections within our domain; however, the predictions are qualitatively similar on all the applied meshes.

From our analysis of temporally and spatially averaged fields, we have deduced the length of the bubble wake region, as displayed in Table V. Our examination of the fields depicted in Fig. 12 focused on the region near the bubble's rear end. We defined the bubble wake length when the magnitude of the observed field diminished to less than 5% of its peak value. Examining the data in Table V, it is apparent that the wake's length primarily depends on the mesh size when considering streamwise velocity fluctuations. This trend is expected, as turbulence is predominantly strong in this direction. Specifically, the coarser G20 mesh appears to suppress turbulence, a pattern also visible in the streamwise velocity component. However, this trend does not hold for radial velocity fluctuations, where the wake length remains consistent across all three mesh sizes. This suggests that the size of the recirculation zone remains unaffected by the mesh size.

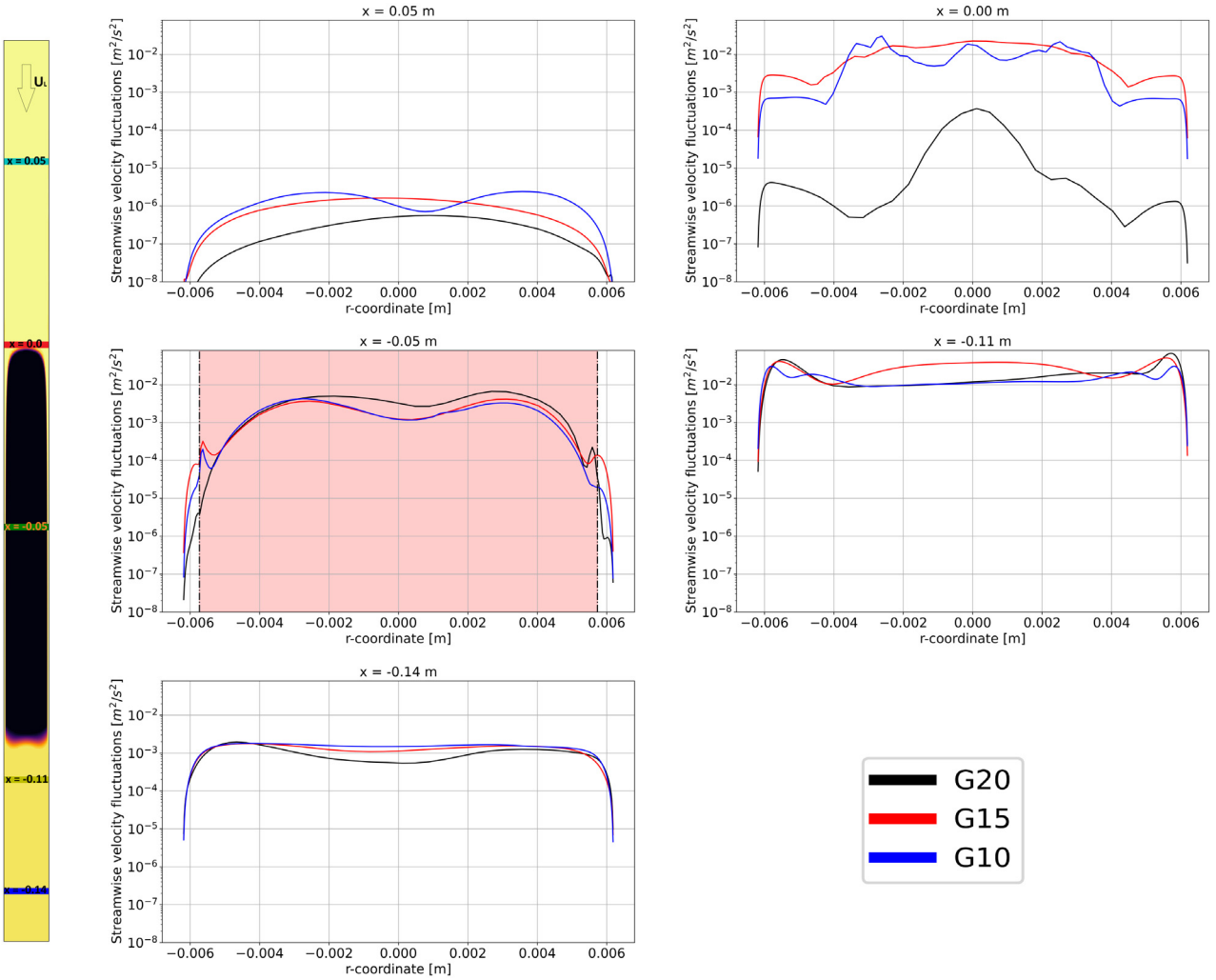

FIG. 8. Streamwise velocity fluctuations profile of a Taylor bubble in counter-current flow. The left side of the figure presents a 2D schematic of a Taylor bubble with denoted different cross sections. The right side displays five one-dimensional plots of streamwise velocity fluctuations, arranged in two rows, corresponding to the cross sections around the Taylor bubble.

We have shown that the Taylor bubble forms a discontinuity in the flow with large gradients in the velocity field, which generate a conducive environment for turbulence generation. The occurrence of turbulence, particularly behind the bubble, can significantly influence the overall flow behavior, affecting everything from bubble breakup and coalescence to heat and mass transfer characteristics.

IV. DISCUSSION: TAYLOR BUBBLE IN TURBULENT COUNTER-CURRENT FLOW

It has been shown in Sec. III that the PLIC VOF method with Runge–Kutta time-integration successfully predicted Taylor bubble behavior, velocity fields, and large-scale structures for the transitional flow regime, where the laminar flow upstream the bubble turns to turbulent in the bubble wake region. In the present section, we use the VOF methods to tackle the dynamics of the Taylor bubble in a fully turbulent regime, which is characterized by chaotic and stochastic flow patterns where inertial forces dominate over viscous forces. In this case, we simulate the Taylor bubble in a larger pipe with a diameter of 26 mm, which, due to its higher Reynolds number of 5600, falls within the turbulent flow regime. Experiments[12] have shown that the Taylor bubble in this flow regime gradually disintegrates, due to the breakup of small bubbles at the tail of the Taylor bubble. The Taylor bubble decay rate depends on the bubble length, pressure, and temperature of the system. For the case, considered in this section, the measured bubble decay rate in the range from 0.015 to 0.07 mm/s is expected.

This study employed the same numerical methods as discussed in Sec. II. The mesh, referred to as G30, has a spanwise bulk cell size of 30 wall units and a near-wall normal cell size of approximately 1 wall unit, altogether consisting of roughly 700 000 cells. Depicted in Fig. 13 are isosurfaces at $\alpha = 0.5$ that represent the instantaneous gas void

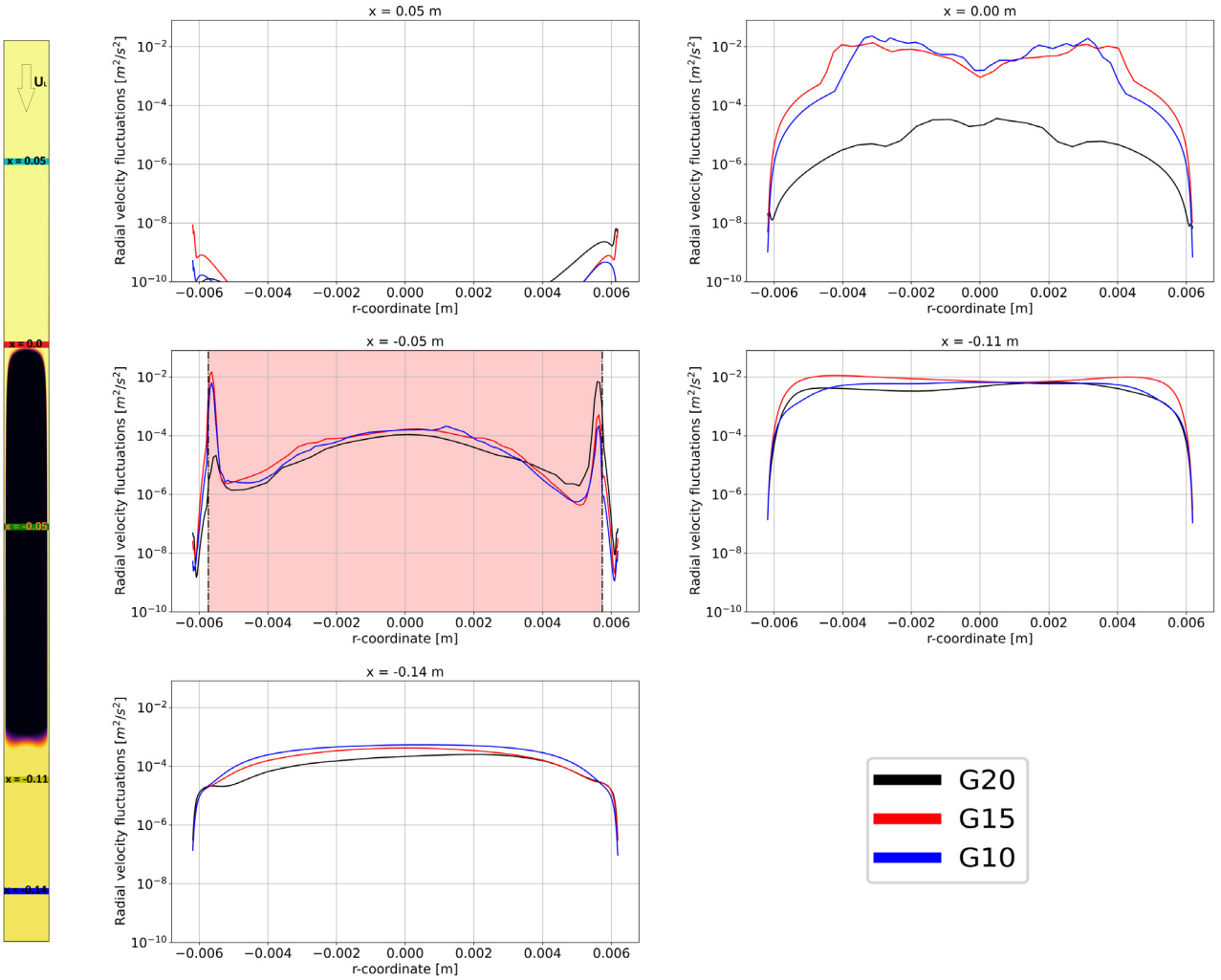

FIG. 9. Radial velocity fluctuations profiles of a Taylor bubble. The left side of the figure presents a 2D schematic of a Taylor bubble with denoted different cross sections. The right side displays five one-dimensional plots of radial velocity fluctuations, arranged in two rows, corresponding to the cross sections around the Taylor bubble.

fraction under turbulent conditions, using two distinct interface capturing methods. The displayed state is $t = 2.2$ s after the simulation's initiation. The simulation was initialized with a fully developed single phase turbulent flow in which a bubble was placed with an initial (theoretical) shape. A key observation is that the highest velocities manifest at the bubble's skirt, progressively leading to bubble breakup. This fragmentation is notably more intense and rapid when using the algebraic capturing method, as evidenced by the abundance of smaller bubbles trailing the main Taylor bubble. In the experimental image on the left, the flow configuration matches that of the numerical simulations, exhibiting less bubble shedding and an asymmetric bubble, a phenomenon also observed in the simulations.

Our analysis has extended for bubble size distributions. Figure 14 presents a histogram of bubble size distribution for G30 mesh and each interface capturing method. The Taylor bubble volume is represented with the column at the most right side of the graph to which the distribution is normalized. In the turbulent flow regime, bubble shedding characteristics exhibited notable differences between the algebraic VOF and PLIC methods. The algebraic VOF method, once again, displayed more pronounced bubble shedding, contributing to a wider bubble size distribution. Conversely, the PLIC method, with its enhanced representation of the interface curvature, limited bubble shedding to a certain extent, resulting in a narrower bubble size distribution. The behavior observed for the PLIC method can be ascribed to a more faithful representation of surface tension forces, reducing artificial fragmentation of the bubbles; however, the predicted bubble decay rate is still one to two orders of magnitude too large with respect to the experimentally measured value.

These results highlight the importance of accurately determining the bubble shape, as it greatly influences the breakup and coalescence rates. As we aim for more precise interface capturing schemes, it becomes evident that additional models for bubble breakup and

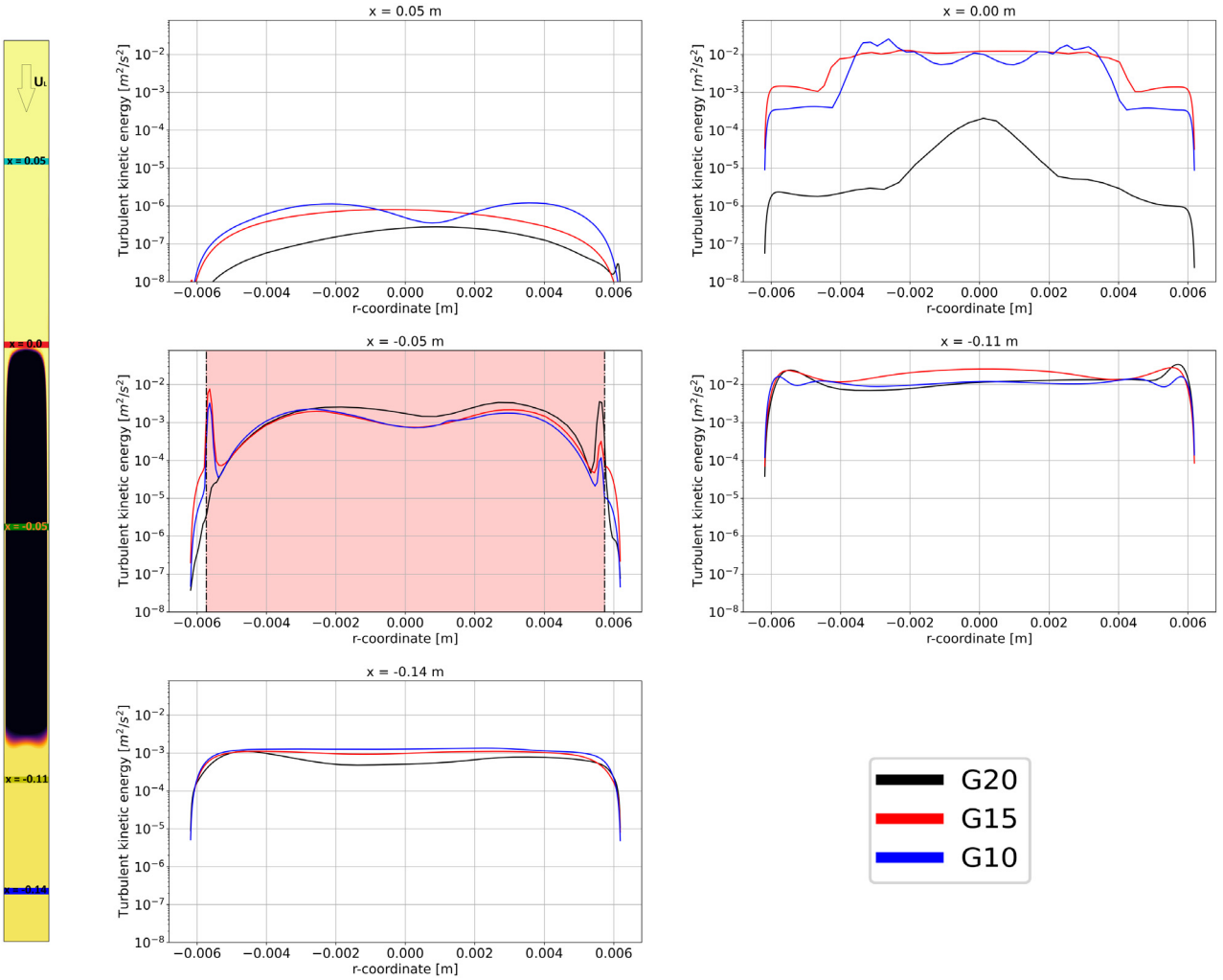

FIG. 10. Turbulent kinetic energy profiles of a Taylor bubble. The left side of the figure presents a 2D schematic of a Taylor bubble with denoted different cross sections. The right side displays five one-dimensional plots of turbulent kinetic energy, arranged in two rows, corresponding to the cross sections around the Taylor bubble.

coalescence should be concurrently developed to enhance the simulation accuracy. However, comparison with experimental results shows that in the turbulent regime the proposed solutions are not sufficient. Taylor bubble in the turbulent regime with the initial size $8-9D_h$ breaks up completely in 20 s in numerical simulations with the PLIC VOF method, but lasts several hours in the experiments. The bubble breakup at the tail of the Taylor bubble is therefore still two orders of magnitude too high.

The primary issue stems from the interactions between the liquid–gas interface, leading to nonphysical outcomes in our numerical simulations. It is important to note that symmetry breaking is an important part of this difficulties. In the turbulent regime as observed in the previous experimental studies by Fabre and Figueroa-Espinoza,[53] and Kren *et al.*,[13] the bubble becomes asymmetric. The numerical simulations further exaggerate this asymmetry, leading to challenges such as the bubble "sticking" to the wall due to factors such as mesh refinement, significant interface deformations, and numerical instabilities. These problems are more pronounced with the algebraic VOF. The VOF with PLIC improves the behavior but does not prevent bubble sticking and the consecutive enhanced breakup. While this topic extends beyond the current paper's scope, it is a key focus for our future research.

V. CONCLUSION

In this study, we have highlighted the significant impact of the choice of interface capturing method on the simulation of multiphase flows, particularly those involving bubble dynamics in a transitional and turbulent slug flow regime. The two methods under consideration were the algebraic VOF method and the geometric, specifically, Piecewise Linear Interface Calculation (PLIC) method. The methods have been applied together with Runge–Kutta time-integration in the newly developed state-of-the-art OpenFOAM solver interRKFoam.

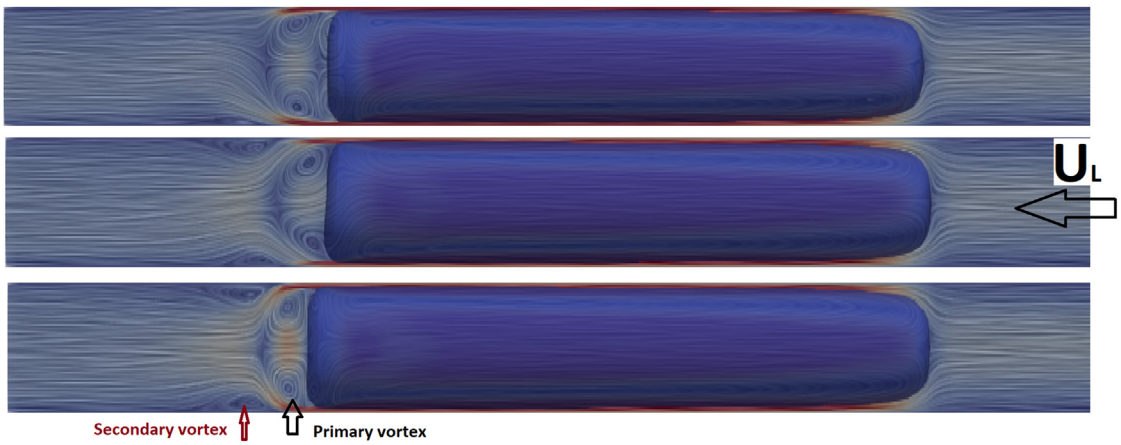

FIG. 11. 2D streamlines of flow behind Taylor bubble. Top: G20 mesh, middle: G15 mesh and bottom: G10 mesh.

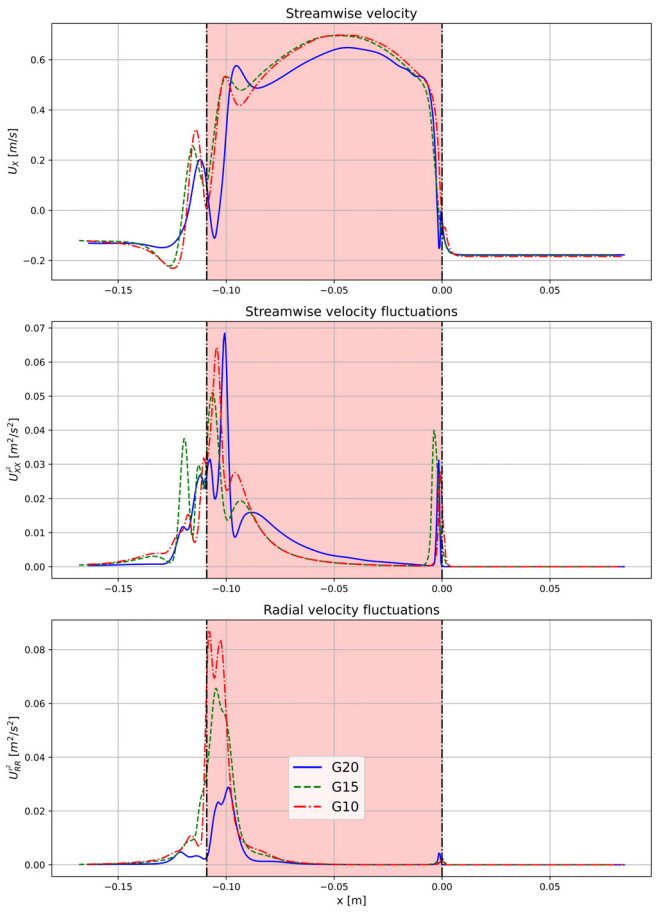

FIG. 12. One-dimensional plots on the pipe axis of streamwise velocity (top), streamwise velocity fluctuations (middle), and radial velocity fluctuations (bottom).

Our analysis showcased a substantial difference in the prediction of bubble breakup between these two methods. The algebraic VOF method demonstrated a more pronounced tendency for bubble breakup, resulting in a broader bubble size distribution. In contrast, the PLIC method showed less bubble breakup, which is in a better agreement with the experimental observations. This difference in behavior is primarily attributed to the more accurate representation of the interface curvature by the PLIC method, which is emphasized especially at locations with large interface curvatures. We have also shown that the algebraic VOF method tended to generate enhanced chaotic behavior due to excessive bubble fragmentation in the turbulent wake region, which was not the case for the geometric VOF.

The LES simulation of the Taylor bubble in a counter-current flow regime with laminar to turbulent transitional Reynolds number of about 1400 has been performed for the first time. The results showed an interesting velocity field downstream the Taylor bubble, which exhibits similarities with the flow characteristics observed downstream a backward-facing step, e.g., the strong separation and wake region. However, besides the formation of the primary toroidal vortex, i.e., the wake region, our findings highlight the formation of a secondary counter-rotating toroidal vortex in the turbulent wake region. The latter vortex turns out to be particularly

TABLE V. Bubble wake length measured with mean velocity and velocity fluctuations for PLIC method.

Mesh	Bubble wake length (in D_h)		
	Streamwise velocity	Streamwise velocity fluctuations	Radial velocity fluctuations
G20	2.90	2.01	1.88
G15	3.20	3.31	1.88
G10	3.28	3.31	1.88

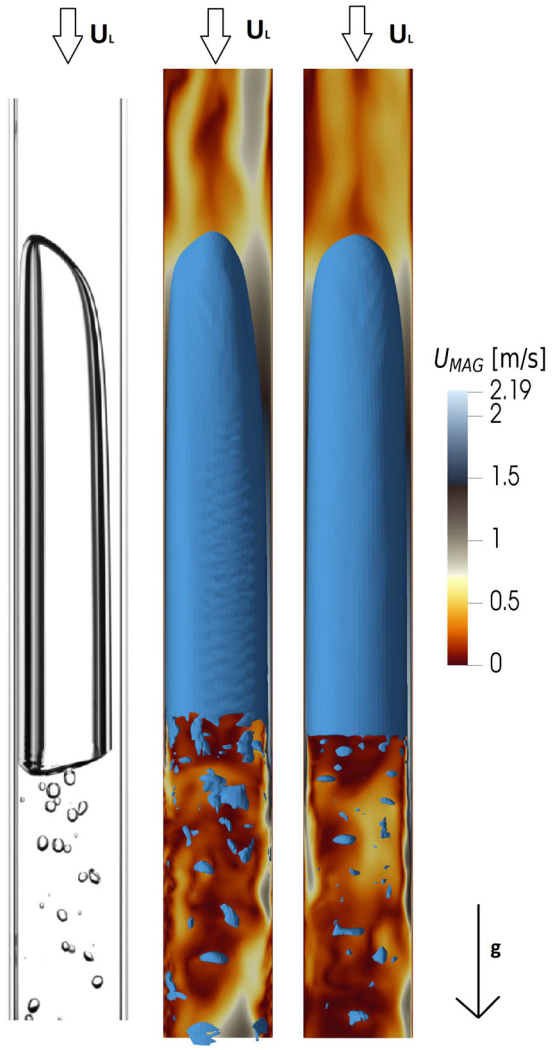

FIG. 13. Isosurfaces of the instantaneous gas void fraction 2.2 s after the initial state obtained with standard algebraic interface capturing (middle) and PLIC reconstruction (right) for turbulent case ($Re = 5600$). The color scheme in the liquid phase represents the velocity magnitude. On the left side, the experimental image displays the flow in the same configuration.

sensitive to the mesh resolution. In addition to the mean velocity, the velocity fluctuations and turbulent kinetic energy have been analyzed for the geometric interface capturing methods. Additionally, the turbulent wake has been analyzed, and it turns out that the length varies between 1.9 and $3.3D_h$ depending on different applied criteria.

In conclusion, while both algebraic and geometric VOF methods serve their purpose depending on the specific requirements of the simulation, it is evident from this study that the geometric VOF, particularly the PLIC method, offers more accurate predictions in cases where the bubble interactions, such as breakup and coalescence, are of interest. However, the PLIC method has its limitations, and it has been shown that for large Reynolds numbers even the PLIC method is not

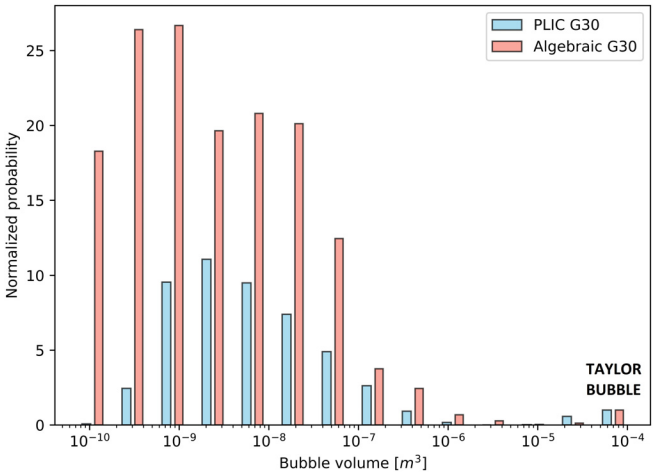

FIG. 14. Bubble distribution sizes for turbulent case.

sufficient for correct determination of bubble breakup and coalescence. Thus, as a future work, the development of additional models is needed, which will better reproduce the bubble dynamics.

ACKNOWLEDGMENTS

The authors gratefully acknowledge financial support provided by Slovenian Research Agency (Grant No. P2-0026) and grant for young researcher Jan Kren.

AUTHOR DECLARATIONS

Conflict of Interest

The authors have no conflicts to disclose.

Author Contributions

Jan Kren: Conceptualization (equal); Data curation (lead); Formal analysis (equal); Investigation (lead); Methodology (equal); Software (equal); Visualization (lead); Writing – original draft (lead). **Edo Frederix:** Conceptualization (equal); Data curation (equal); Formal analysis (equal); Methodology (equal); Software (equal); Writing – review & editing (equal). **Iztok Tiselj:** Conceptualization (equal); Resources (equal); Writing – review & editing (equal). **Blaž Mikuž:** Conceptualization (equal); Investigation (equal); Methodology (equal); Resources (equal); Writing – original draft (equal).

DATA AVAILABILITY

OpenFOAM solver interRKFoam is published under the GNU GPL Version 3 license at the following URL https://repo.ijs.si/kren/interrkfoam. Simulation data and computer codes used for data post-processing are available from the corresponding author upon reasonable request.

APPENDIX: VERIFICATIONS TESTS

To ensure the accuracy and reliability of our simulation results, we conducted a rigorous process of verification. This was needed as

FIG. 15. interRKFoam solver. Left column: algebraic, middle: PLIC, right: MPLIC interface capturing method. Top row: after one rotation, bottom: after five rotations. Mesh size: 100 × 100.

the used solver was modified significantly with respect to the basic interFoam solver.

The first verification case was the Zalesak disk case, a standard test problem for advection schemes that involves the transport of a slotted disk shape by a rotating velocity field. This case tests the ability of our advection scheme to preserve the sharpness of interfaces and to avoid numerical diffusion and oscillations.

We compared our simulation results for the Zalesak disk case between different interface capturing methods in terms of the shape and location of the transported disk after one rotation and after five rotations as shown in Figs. 15 and 16. We have used two different meshes; i.e., 100 × 100 cells and 500 × 500 cells. Our results showed that geometric reconstruction schemes (PLIC and MPLIC) improve the results of the advection. MPLIC, short for Multicut Piecewise Linear Interface Capturing, represents an extended version of PLIC that is able to perform multiple cuts within a single line. After a single rotation of the disk, it is challenging to determine which reconstruction is the best (regardless of mesh density). However, after five rotations, it becomes evident that both PLIC and MPLIC perform better as they cause less deformation to the shape of the slotted disk. Generally, superior results are achieved with denser discretization meshes, yet even with these, undesired artifacts such as surface wrinkles can occur. The difference between PLIC and MPLIC method is minimal, and therefore, we have decided that MPLIC is not worth the additional computational cost.

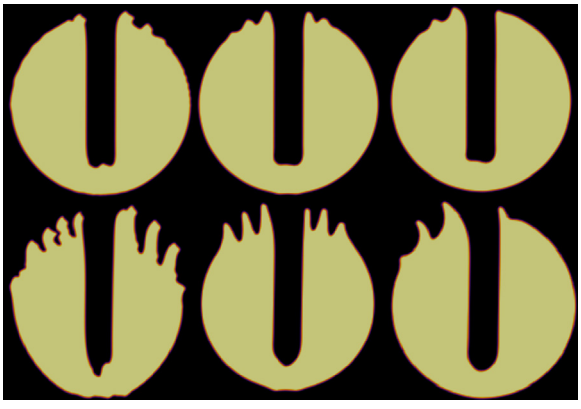

FIG. 16. interRKFoam solver. Left column: algebraic, middle: PLIC, right: MPLIC interface capturing method. Top row: after one rotation, bottom: after five rotations. Mesh size: 500 × 500.

The second verification case we considered was the Hysing benchmark case,[54–56] a well-known test for multiphase flow simulations that involves the rising and deformation of a single bubble in a quiescent fluid (see Fig. 17). We have employed the second of the two Hysing tests and the chosen mesh was intentionally coarse to enhance the clarity of the distinctions. This case provides a stringent test of our simulation's ability to accurately capture the dynamics of bubble motion, including effects such as buoyancy, surface tension, and the interaction of the bubble with the surrounding fluid. The ratio of densities in this case is 1000, the ratio of kinematic viscosity is 0.1, and surface tension is 1.96 kg/s^2.

Our simulation results for the Hysing case were compared with the standard interFoam solver and with benchmark simulations as provided in the paper by Klostermann *et al.*[55] in terms of the key parameters such as the bubble rise velocity, the shape of the deforming bubble, and the bubble circularity. The circularity is determined as the ratio of the bubble area multiplied by 4π, to the square of the bubble's perimeter $circularity = \frac{4\pi A}{P^2}$. The interRKFoam solver has been used with the second-order DIRK2 time integration scheme, whereas the interFoam solver has been used with the first-order Backward Euler time integration scheme. In both cases, we have used PLIC reconstruction scheme. The comparison is shown in Table VI. We demonstrate the discrepancies among interRKFoam, interFoam, and the reference case by comparing the maximum velocity of the bubble V_{max}, the time at which this peak velocity is reached $t(V_{max})$, and the bubble's circularity at $t = 3$ s. The case provides the difference in the mentioned properties

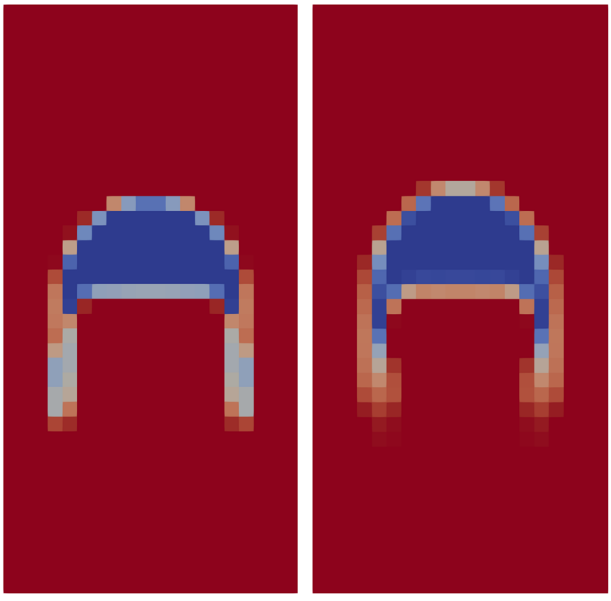

FIG. 17. Hysing benchmark case—left interFoam, right interRKFoam at $t = 3$ s.

TABLE VI. Comparison of the Hysing benchmark case data.

Case	Area	V_{max}	$t(V_{max})$	Circularity
interFoam	0.113	0.2492	0.758	0.70
interRKFoam	0.107	0.2429	0.756	0.74
Reference	···	0.2474	0.7156	0.72

in the range of 10% for different used codes as shown by Klostermann *et al.*[55] This is most obvious in the case of circularity, where we can observe two different evolutions. In one case, the bubble remains skirted with elongated filaments, and in the other case (interFoam and interRKFoam are of such instance), there is a separation of satellite bubbles, i.e., bubble breakup. This difference is documented by a very different evolution of circularity, where the circularity drops to around 0.5 if the bubble stays skirted or increases to the value around 0.7 if the filaments detach. This can also be seen in Fig. 17. We have chosen to highlight the results on the 100×100 mesh specifically because the differences are most pronounced at this resolution. The comparison showed that our simulation results closely matched the interFoam solver, indicating that our computational methods and implementations were working correctly. When going back to Backward Euler scheme with interRKFoam the results were the same as with interFoam.

Through these verification cases, we have gained confidence in the correctness of our computational methods and their implementation in our simulations.

REFERENCES

[1]S. B. Pope, *Turbulent Flows* (Cambridge University Press, Cambridge, New York, 2000).
[2]R. T. Lahey, E. Baglietto, and I. A. Bolotnov, "Progress in multiphase computational fluid dynamics," Nucl. Eng. Des. **374**, 111018 (2021).
[3]G. Tryggvason, R. Scardovelli, and S. Zaleski, *Direct Numerical Simulations of Gas-Liquid Multiphase Flows* (Cambridge University Press, Cambridge, NY, 2011).
[4]G. Zhou and A. Prosperetti, "Violent expansion of a rising Taylor bubble," Phys. Rev. Fluids **4**, 073903 (2019).
[5]Y. Liao and D. Lucas, "A literature review of theoretical models for drop and bubble breakup in turbulent dispersions," Chem. Eng. Sci. **64**, 3389–3406 (2009).
[6]Z.-S. Mao and A. Dukler, "The motion of Taylor bubbles in vertical tubes—II. Experimental data and simulations for laminar and turbulent flow," Chem. Eng. Sci. **46**, 2055–2064 (1991).
[7]A. Pinto, M. Coelho Pinheiro, S. Nogueira, V. Ferreira, and J. Campos, "Experimental study on the transition in the velocity of individual Taylor bubbles in vertical upward co-current liquid flow," Chem. Eng. Res. Des. **83**, 1103–1110 (2005).
[8]L. Shemer, A. Gulitski, and D. Barnea, "Experiments on the turbulent structure and the void fraction distribution in the Taylor bubble wake," Multiphase Sci. Technol. **17**, 103–122 (2005).
[9]L. Shemer, A. Gulitski, and D. Barnea, "On the turbulent structure in the wake of Taylor bubbles rising in vertical pipes," Phys. Fluids **19**, 035108 (2007).
[10]R. F. Cerqueira and E. E. Paladino, "Experimental study of the flow structure around Taylor bubbles in the presence of dispersed bubbles," Int. J. Multiphase Flow **133**, 103450 (2020).
[11]S. Benattalah, F. Aloui, and M. Souhar, "Experimental analysis on the counter-current Dumitrescu-Taylor bubble flow in a smooth vertical conduct of small diameter," J. Appl. Fluid Mech. **4**, 1–14 (2011).
[12]B. Mikuž, J. Kamnikar, J. Prošek, and I. Tiselj, "Experimental observation of Taylor bubble disintegration in turbulent flow," in *Proceedings of the 28th International Conference Nuclear Energy for New Europe, Slovenia* (Nuclear Society of Slovenia, 2019), p. 9.
[13]J. Kren, B. Zajec, I. Tiselj, S. E. Shawish, Z. Perne, M. Tekavcic, and B. Mikuz, "Dynamics of Taylor bubble interface in vertical turbulent counter-current flow," Int. J. Multiphase Flow **165**, 104482 (2023).
[14]K. Tsuchiya and H. Brenner, *Bubble Wake Dynamics in Liquids and Liquid-Solid Suspensions* (Elsevier Science, St. Louis, 1990).
[15]P. Ghosh, "Coalescence of bubbles in liquid," Bubble Sci. Eng. Technol. **1**, 75–87 (2009).
[16]T. Morokuma and Y. Utaka, "Variation of the liquid film thickness distribution between contacting twin air bubbles during the coalescence process in water and ethanol pools," Int. J. Heat Mass Transfer **98**, 96–107 (2016).
[17]J.-W. Park, D. Drew, and R. Lahey, "The measurement of void waves in bubbly two-phase flows," Nucl. Eng. Des. **149**, 37–52 (1994).
[18]Y. Qi, A. U. Mohammad Masuk, and R. Ni, "Towards a model of bubble breakup in turbulence through experimental constraints," Int. J. Multiphase Flow **132**, 103397 (2020).
[19]P. Chu, J. Finch, G. Bournival, S. Ata, C. Hamlett, and R. J. Pugh, "A review of bubble break-up," Adv. Colloid Interface Sci. **270**, 108–122 (2019).
[20]Y. Liao and D. Lucas, "A literature review on mechanisms and models for the coalescence process of fluid particles," Chem. Eng. Sci. **65**, 2851–2864 (2010).
[21]C. T. Crowe, T. R. Troutt, and J. N. Chung, "Numerical models for two-phase turbulent flows," Annu. Rev. Fluid Mech. **28**, 11 (1996).
[22]M. F. Trujillo, "Reexamining the one-fluid formulation for two-phase flows," Int. J. Multiphase Flow **141**, 103672 (2021).
[23]C. Hirt and B. Nichols, "Volume of fluid (VOF) method for the dynamics of free boundaries," J. Comput. Phys. **39**, 201–225 (1981).
[24]M. Sint Annaland, N. Deen, and J. Kuipers, "Numerical simulation of gas bubbles behaviour using a three-dimensional volume of fluid method," Chem. Eng. Sci. **60**, 2999–3011 (2005).
[25]S. Osher and R. P. Fedkiw, "Level set methods: An overview and some recent results," J. Comput. Phys. **169**, 463–502 (2001).
[26]The OpenFOAM Foundation, *OpenFOAM | Free CFD Software* (The OpenFOAM Foundation, 2022).
[27]P. Cifani, W. Michalek, G. Priems, J. Kuerten, C. Geld, and B. Geurts, "A comparison between the surface compression method and an interface reconstruction method for the VOF approach," Comput. Fluids **136**, 421–435 (2016).
[28]D. Dai and A. Y. Tong, "Analytical interface reconstruction algorithms in the PLIC–VOF method for 3D polyhedral unstructured meshes," Numer. Methods Fluids **91**, 213–227 (2019).
[29]S. C. De Schepper, G. J. Heynderickx, and G. B. Marin, "CFD modeling of all gas–liquid and vapor–liquid flow regimes predicted by the Baker chart," Chem. Eng. J. **138**, 349–357 (2008).
[30]S. Ketterl, M. Reißmann, and M. Klein, "Large eddy simulation of multiphase flows using the volume of fluid method: Part 2 – A-posteriori analysis of liquid jet atomization," Exp. Comput. Multiphase Flow **1**, 201–211 (2019).
[31]M. Klein, S. Ketterl, and J. Hasslberger, "Large eddy simulation of multiphase flows using the volume of fluid method: Part 1—Governing equations and a priori analysis," Exp. Comput. Multiphase Flow **1**, 130–144 (2019).
[32]R. D. Moser, S. W. Haering, and G. R. Yalla, "Statistical properties of subgrid-scale turbulence models," Annu. Rev. Fluid Mech. **53**, 255–286 (2021).
[33]A. W. Vreman, "An eddy-viscosity subgrid-scale model for turbulent shear flow: Algebraic theory and applications," Phys. Fluids **16**, 3670–3681 (2004).
[34]M. Saeedipour and S. Schneiderbauer, "Favre-filtered LES-VOF of two-phase flows with eddy viscosity-based subgrid closure models: An *a-posteriori* analysis," Int. J. Multiphase Flow **144**, 103780 (2021).
[35]M. Saeedipour and S. Schneiderbauer, "A new approach to include surface tension in the subgrid eddy viscosity for the two-phase LES," Int. J. Multiphase Flow **121**, 103128 (2019).
[36]M. Saeedipour, S. Vincent, S. Pirker, and S. Schneiderbauer, "Towards a general structural subgrid modelling approach for turbulent multiphase flows," in *10th International Conference on Multiphase Flow, Brazil* (ICMF, 2019), p. 3.
[37]J. Araújo, J. Miranda, A. Pinto, and J. Campos, "Wide-ranging survey on the laminar flow of individual Taylor bubbles rising through stagnant Newtonian liquids," Int. J. Multiphase Flow **43**, 131–148 (2012).
[38]A. Morgado, J. Miranda, J. Araújo, and J. Campos, "Review on vertical gas–liquid slug flow," Int. J. Multiphase Flow **85**, 348–368 (2016).

[39]R. F. Cerqueira, E. E. Paladino, F. Evrard, F. Denner, and B. Wachem, "Multiscale modeling and validation of the flow around Taylor bubbles surrounded with small dispersed bubbles using a coupled VOF-DBM approach," Int. J. Multiphase Flow **141**, 103673 (2021).
[40]E. Gutiérrez, N. Balcázar, E. Bartrons, and J. Rigola, "Numerical study of Taylor bubbles rising in a stagnant liquid using a level-set/moving-mesh method," Chem. Eng. Sci. **164**, 158–177 (2017).
[41]B. Mikuž, E. M. A. Frederix, E. M. J. Komen, and I. Tiselj, "Taylor bubble behaviour in turbulent flow regime," in *Proceedings of the Conference Computational Fluid Dynamics for Nuclear Reactor Safety (CFD4NRS-8)* (EUROMECH, 2020), p. 12.
[42]M. L. Talley, M. D. Zimmer, and I. A. Bolotnov, "Coalescence prevention algorithm for level set method," J. Fluids Eng. **139**, 081301 (2017).
[43]M. Kwakkel, W.-P. Breugem, and B. J. Boersma, "Extension of a CLSVOF method for droplet-laden flows with a coalescence/breakup model," J. Comput. Phys. **253**, 166–188 (2013).
[44]S. Schwarz, S. Tschisgale, and J. Fröhlich, "Bubble coalescence model for phase-resolving simulations using an immersed boundary method," in *Joint EUROMECH / ERCOFTAC Colloquium 549, Leiden* (OECD/NEA, 2013), p. 5.
[45]E. M. A. Frederix, E. M. J. Komen, I. Tiselj, and B. Mikuž, "LES of turbulent co-current Taylor bubble flow," Flow Turbul. Combust. **105**, 471–495 (2020).
[46]J. Brackbill, D. Kothe, and C. Zemach, "A continuum method for modeling surface tension," J. Comput. Phys. **100**, 335–354 (1992).
[47]C. A. Kennedy and M. H. Carpenter, "Diagonally implicit Runge-Kutta methods for ordinary differential equations. A review," Report No. NASA/TM-2016-219173, 2016.
[48]T. Abadie, J. Aubin, and D. Legendre, "On the combined effects of surface tension force calculation and interface advection on spurious currents within volume of fluid and level set frameworks," J. Comput. Phys. **297**, 611–636 (2015).
[49]S. Popinet, "Numerical models of surface tension," Annu. Rev. Fluid Mech. **50**, 49–75 (2018).
[50]J. L. G. Oliveira, C. W. M. Van Der Geld, and J. G. M. Kuerten, "Lagrangian and Eulerian statistics of pipe flows measured with 3D-PTV at moderate and high Reynolds numbers," Flow Turbul. Combust.**91**, 105–137 (2013).
[51]E. M. A. Frederix, S. Tajfirooz, J. A. Hopman, J. Fang, E. Merzari, and E. M. J. Komen, "Two-phase turbulent kinetic energy budget computation in co-current Taylor bubble flow," Nucl. Sci. Eng. **197**, 2585–2601 (2023).
[52]B. Zajec, M. Matkovič, N. Kosanič, J. Oder, B. Mikuž, J. Kren, and I. Tiselj, "Turbulent flow over confined backward-facing step: PIV vs. DNS," Appl. Sci. **11**, 10582 (2021).
[53]J. Fabre and B. Figueroa-Espinoza, "Taylor bubble rising in a vertical pipe against laminar or turbulent downward flow: Symmetric to asymmetric shape transition," J. Fluid Mech. **755**, 485–502 (2014).
[54]S. Hysing, S. Turek, D. Kuzmin, N. Parolini, E. Burman, S. Ganesan, and L. Tobiska, "Quantitative benchmark computations of two-dimensional bubble dynamics," Numer. Methods Fluids **60**, 1259–1288 (2009).
[55]J. Klostermann, K. Schaake, and R. Schwarze, "Numerical simulation of a single rising bubble by VOF with surface compression," Numer. Methods Fluids **71**, 960–982 (2013).
[56]L. Štrubelj, I. Tiselj, and B. Mavko, "Simulations of free surface flows with implementation of surface tension and interface sharpening in the two-fluid model," Int. J. Heat Fluid Flow **30**, 741–750 (2009).